Supplementary Information (S)

Rapid Scalable One-step Production of Catalysts for Low-Iridium Content Proton Exchange Membrane Water Electrolyzers

Suriya Venkatesan[1,2], Jens Mitzel[1], Sambal Shashank Ambu[1,2,3], Tobias Morawietz[1,4], Indro Biswas[1], Oscar Recalde[5], Esmaeil Adabifiroozjaei[5], Leopoldo Molina-Luna[5], Deven P. Estes[6], Karsten Wegner[7,8], Pawel Gazdzicki[1], Aldo Saul Gago[1,*], and Kaspar Andreas Friedrich[1,2]

[1]Department of Electrochemical Energy Technology, Institute of Engineering Thermodynamics, German Aerospace Centre (DLR), 70569 Stuttgart, Germany

[2]Institute of Building Energetics, Thermal Engineering and Energy Storage (IGTE), University of Stuttgart, 70569 Stuttgart, Germany

[3]Cutting-Edge Nanomaterials (CENmat), 75181 Pforzheim, Germany

[4]Faculty of Science, Energy and Building Services, Esslingen University of Applied Sciences, 73728 Esslingen am Neckar, Germany

[5]Advanced Electron Microscopy Division, Department of Materials- and Geosciences, Technical University Darmstadt, 64287 Darmstadt, Germany

[6]Institute of Technical Chemistry, University of Stuttgart, 70569 Stuttgart, Germany

[7]Particle Technology Laboratory, Department of Mechanical and Process Engineering, ETH Zurich, 8092 Zurich, Switzerland

[8]ParteQ GmbH, 76316 Malsch, Germany

*Corresponding Author: Aldo.Gago@dlr.de

Supporting Information Content

Different samples used for discussing the potential of the FSP-made electrocatalysts for low-loaded PEMWE applications are listed in Table S1.

Table S1: The samples and their key process parameters used for FSP synthesis.

Sample Name	Dispersion-O_2 per 5 ml of precursor (L min^{-1})	Shroud gas, air (L min^{-1})	Quenching gas, air (L min^{-1})
IrO_x	8	80	-
$Sn_{0.9}Sb_{0.1}O_2$	8	80	-
37-ISS	8	80	-
37-ISS-5	5	80	-
37-ISS-2	2	80	-
51-ISS	8	80	-
51-ISS-Q	8	80	60 L min^{-1} introduced at 10 cm above the atomizer. A 10 cm quartz tube was used to prevent uncontrolled particle flow with the introduction of quench gas.

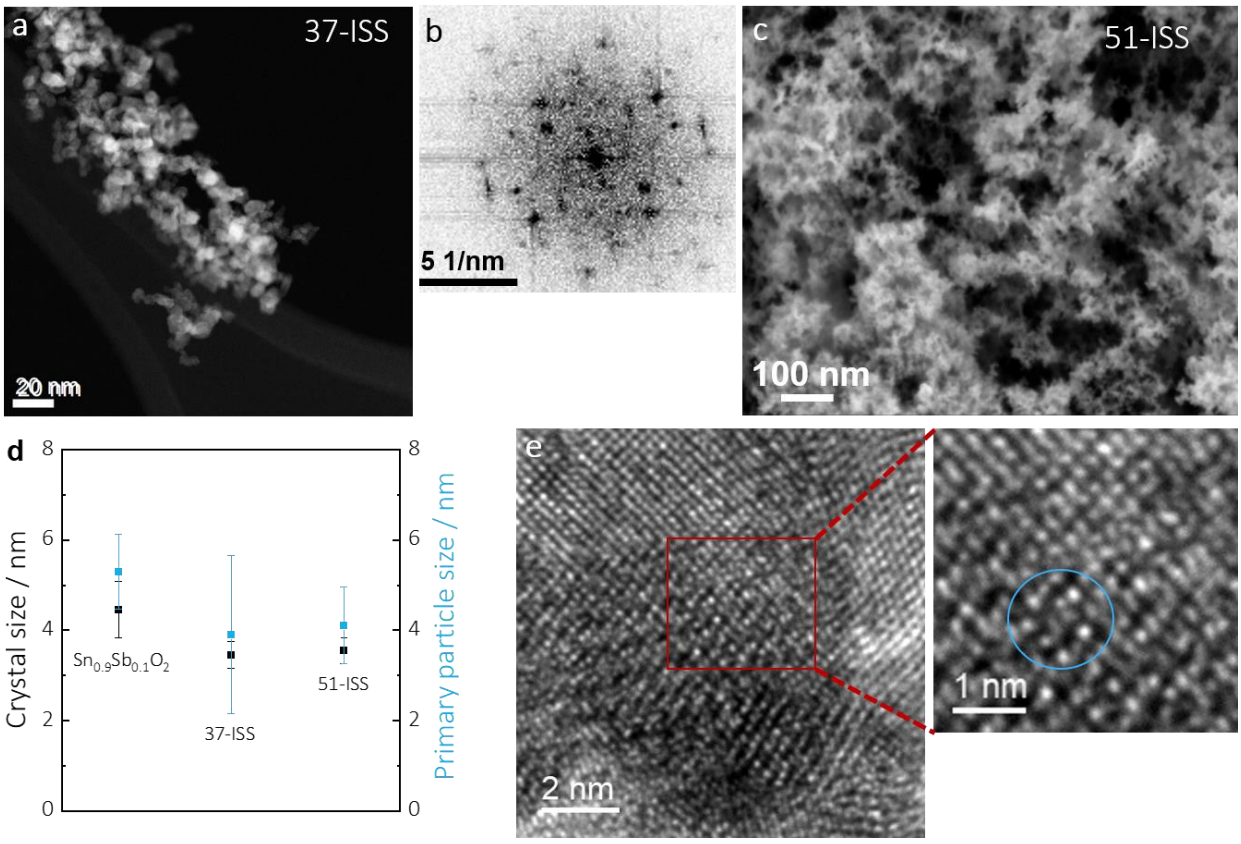

Figure S1: a) Low magnification HAADF-STEM image of 37-ISS. b) Corresponding FFT image on a small area. c) In-lens SEM image of as-synthesized 51-ISS. d) Average crystal size and primary particle size comparison plot for $Sn_{0.9}Sb_{0.1}O_2$, 37-ISS and 51-ISS. e) HR-TEM image of 37-ISS. A zoomed-in image of the red marked area, revealing a nanocrystalline arrangement with defects circled in blue.

The lower geometric standard deviations of primary particles (Fig. S1d) of IrO_x and $Sn_{0.9}Sb_{0.1}O_2$ support the nucleation of both particles through high temperature-induced thermal shock-assisted vapor-phase processes, as reported in the literatures.[1, 2]

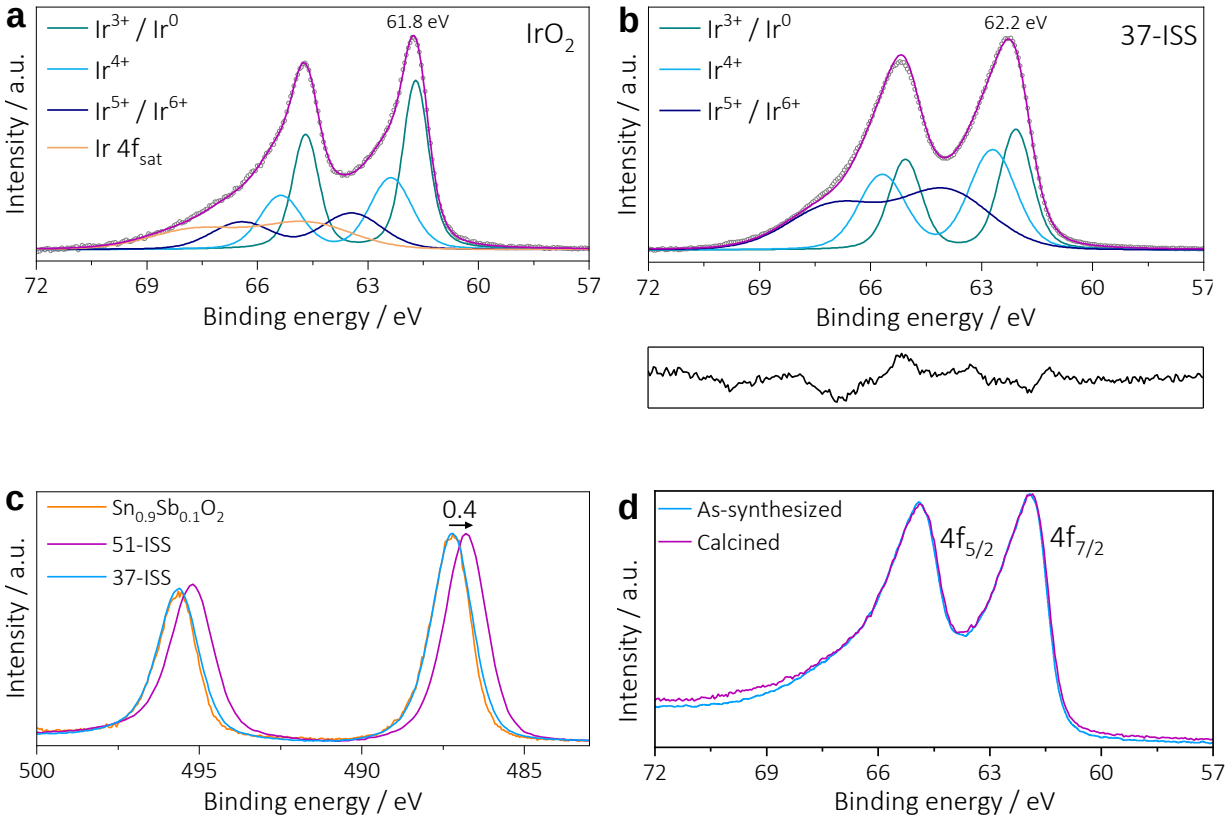

Figure S2: a) Ir4f XPS signals of commercial IrO_2. b) 37-ISS Ir4f XPS signal fittings without satellite peaks. Residual signal at the bottom of the image indicates that with only three signal components, the measured signal is not described sufficiently. c) Sn3d XPS signals of 37-ISS, 51-ISS in comparison with $Sn_{0.9}Sb_{0.1}O_2$. d) Ir4f XPS signals of calcined 37-ISS in comparison with as-synthesized 37-ISS.

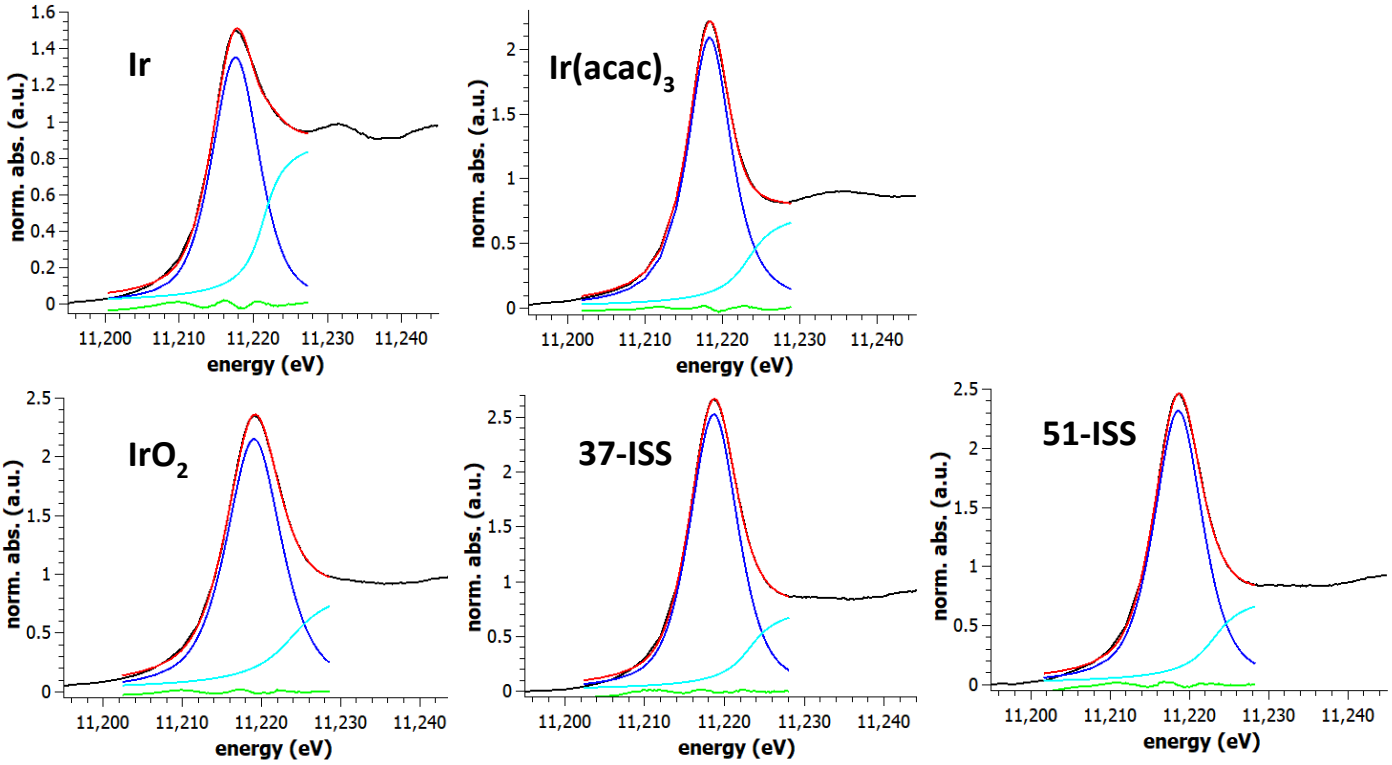

Figure S3: Fitted L3 edge spectrum of Ir metal, $Ir(acac)_3$, IrO_2, 37-ISS, and 51-ISS samples with the different colors representing the experimental data (black), fitted spectrum (red), the pseudo-Voigt function modelling the white-line peak (blue), edge jump (cyan), and residual intensity (green).

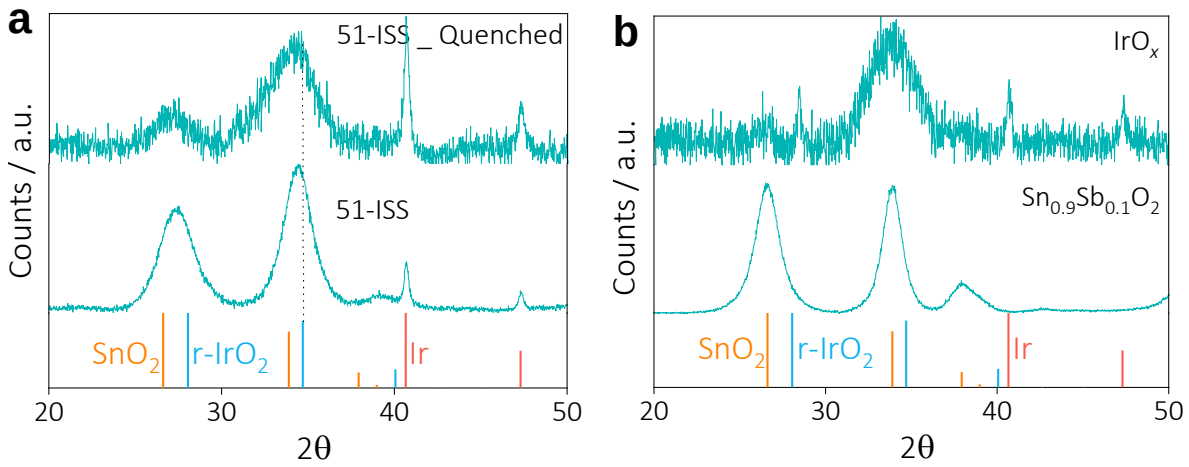

Figure S4: XRD patterns of (a) Quenched 51-ISS-Q compared with unquenched 51-ISS, and (b) IrO_x compared with $Sb_{0.9}Sn_{0.1}O_2$.

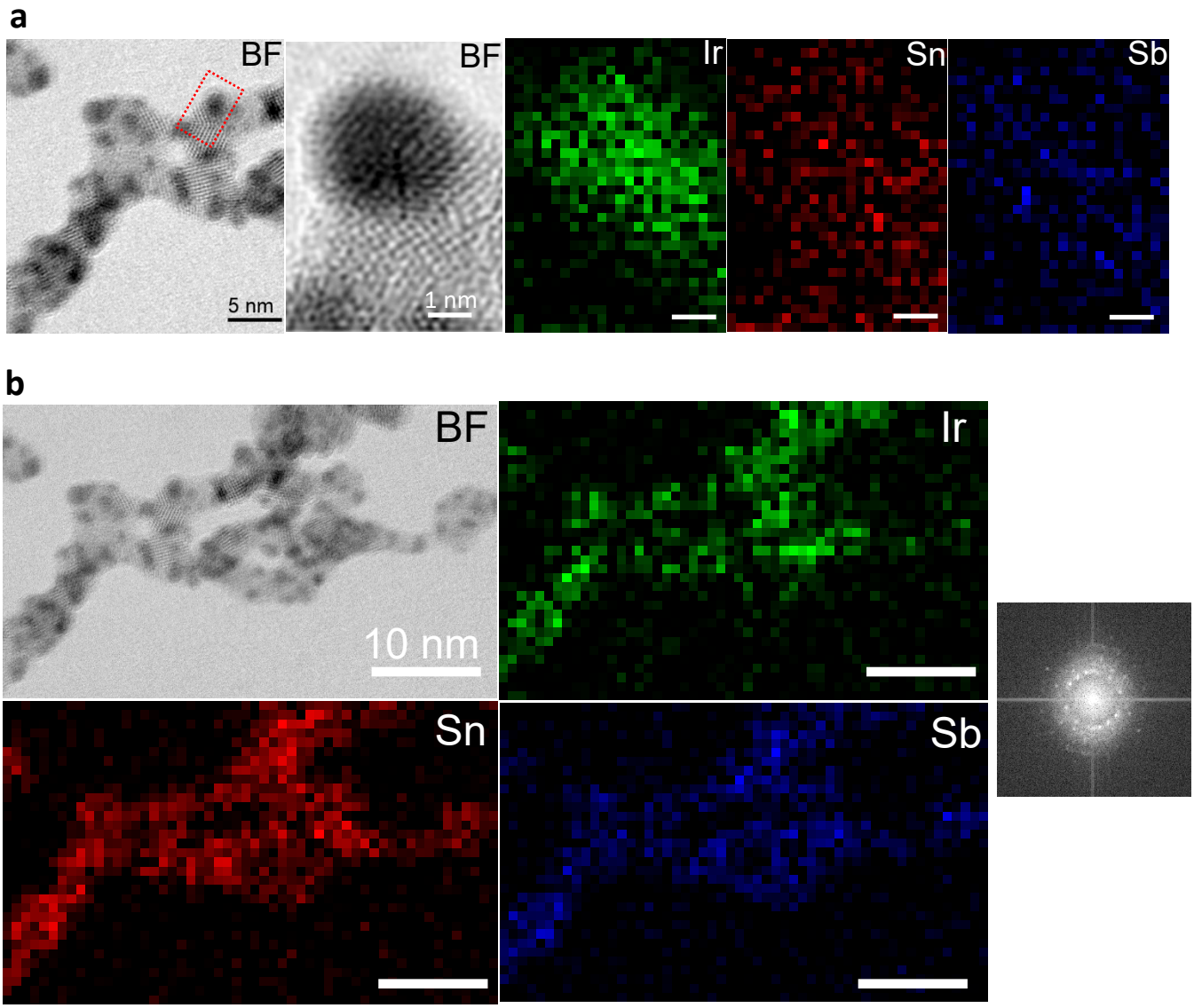

Figure S5: a) Bright field STEM image of 51-ISS with a marked area for high magnification image showing the supported solid solution morphology. Corresponding elemental maps of Ir, Sn and Sb. b) Bright field STEM and corresponding elemental maps of Ir, Sb and Sn, and Corresponding FFT image on a small area from 51-ISS.

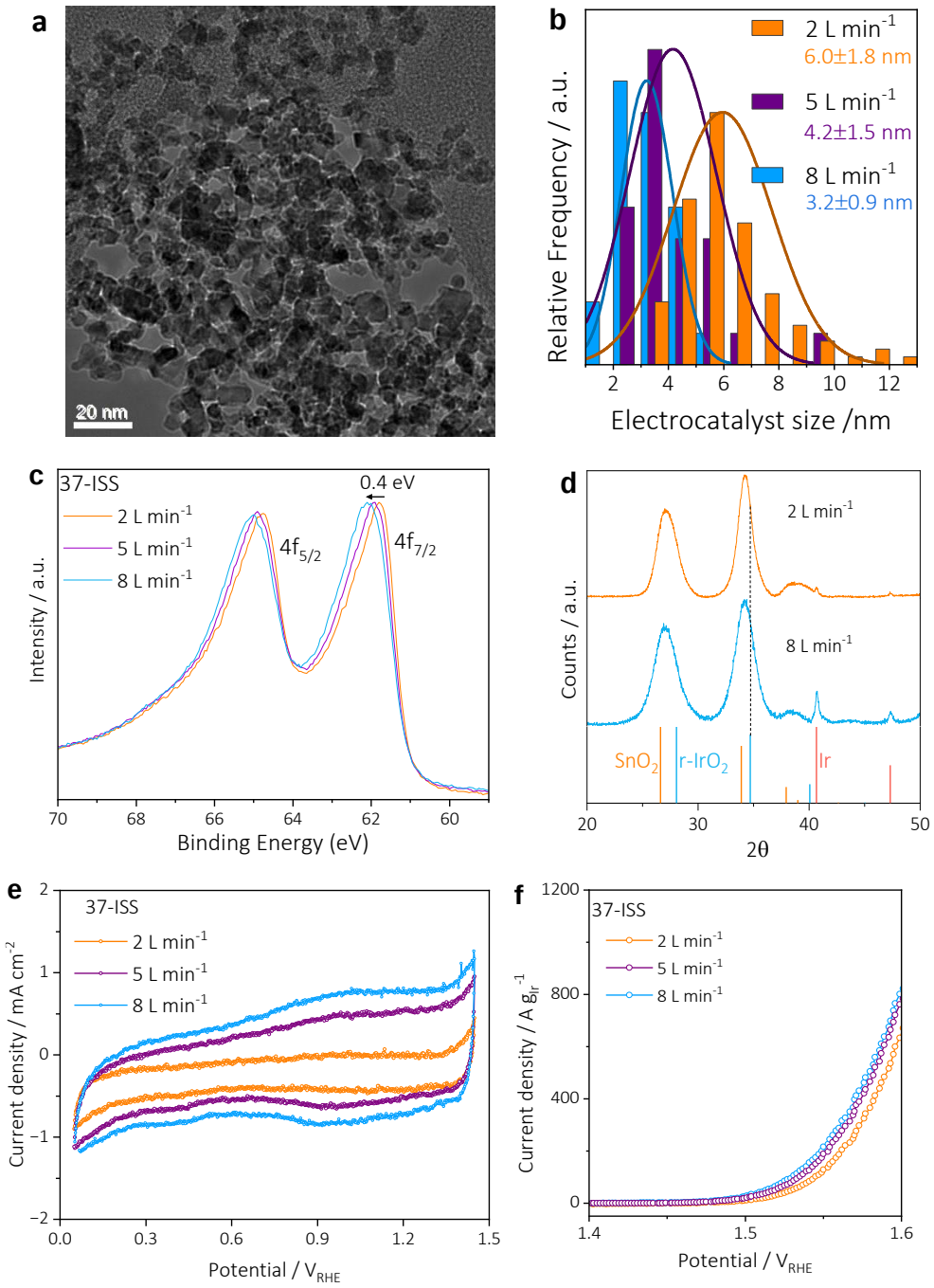

Figure S6: A key strategy for synthesis optimization mechanism in FSP: a) HR-TEM image of 37-ISS produced using 2 L min^{-1} dispersion oxidant gas per 5 mL min^{-1} precursor flow rate. b) Histogram of electrocatalyst size distribution of 37-ISS produced using 2, 5 and 8 L min^{-1} dispersion oxidant gas flow rates per 5 mL min^{-1} of precursor-fuel feed rate. c) Ir4f XPS spectra. d) XRD pattern. e) Cyclic voltammogram. b) Ir-mass normalized OER activity plot.

The versatile FSP technique further allows control over the catalyst particle formation mechanism without significant change in the catalytic activity. For instance, further optimization in synthesis

parameters, such as the precursor composition, precursor to dispersion oxidant ratio, particle residence time in the flame, and shroud gas flow rates, could aid in reducing pure Ir phases and promoting a more homogenous solid solution with higher valent Ir species. Here, a strategy utilizing different dispersion oxidant-to-fuel precursor feed ratios was demonstrated as a key synthesis parameter to fine-tune the particle size, the specific surface area, Ir oxidation state and phase separation, and thus catalytic activity.

37-ISS was produced using dispersion oxygen flow rates of 8, 5 and 2 L min^{-1}, resulting in average particle sizes of (3.2±0.9) nm, (4.2±1.5) nm, and (6.0±1.8) nm, respectively (Fig. S6a-b). The decrease of dispersion oxygen flow at a constant precursor feed rate of 5 mL min^{-1} increased the flame length and thus the time for particle growth. The increased dispersion gas flow decreases the flame temperature and facilitates precursor vapor mixing, ensuring more homogeneous dispersion of elements without phase segregation and promoting the formation of ordered higher valent Ir species. However, these particles lack sufficient residence time in the flame and contain a small fraction of partially oxidized metal phase (Fig. S6d). On the other hand, although decreased dispersion gas flow rates can produce oxidized and grown particles, the lower average oxidation state of Ir indicates presence of more oxygen vacancies (Fig. S6c).

The changes in specific surface area were reflected in the double layer capacitance of the respective samples (Fig. S6e). Typically, a decrease in surface area can have a negative impact on electrochemical performance. However, the flame-derived electrocatalyst demonstrated negligible changes in OER characteristic performance even with a 40% increased particle size (Fig. S6f). This is possible if solubility of different elements increases. Additionally, the presence oxygen vacancies in the catalysts produced at decreased dispersion flow rates could improve catalyst surface wettability[3] and therefore the mass transport properties to the electrocatalysts. Muravev et al.[4, 5] recently reported an approach changing the precursor feed rate to study the size-dependent performance and durability of one-step FSP-made Pd-CeO_2 nanocomposite for CO oxidation. Furthermore, with appropriate synthesis parameters, the authors have validated that the production of atomically dispersed precious metals in a non-precious oxide matrix can be achieved using high temperature FSP methods. Together, both the approaches once again validate the versatility of flame processing in tailoring the materials properties through controlled particle formation mechanism.

It is worth noting that the versatile optimization mechanism not only allows oxidizing metallic Ir with reduced dispersion gas flow of 2 L min^{-1}, but conversely, a larger fraction of metallic Ir can also be retained by quenching the flame, as in the case of 51-ISS-Q (Fig. S4a). The facile quenching strategy resulted in relatively high entropic mixing of Ir (Fig. S7), and as evidenced by a decrease in 2θ of the (101) plane for 51-ISS-Q (Fig. S4a) compared to 51-ISS (unquenched), and an increase in degree of distortion-brought amorphousness.

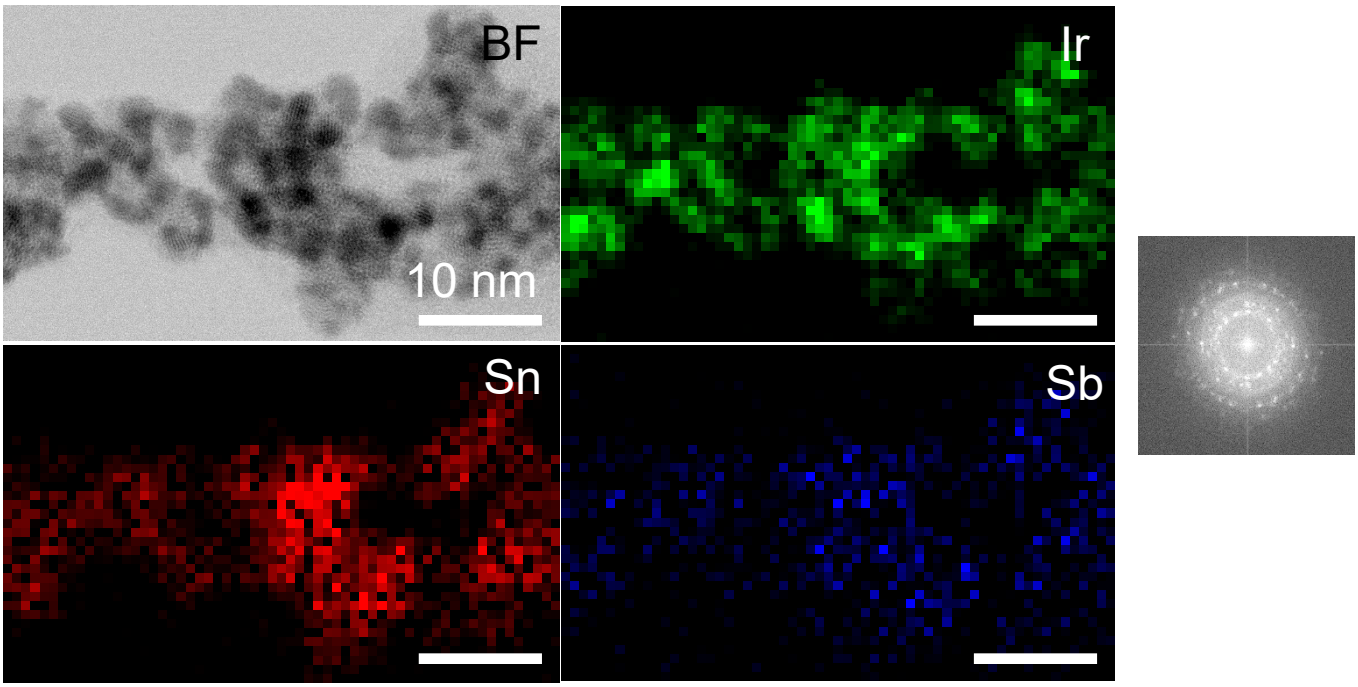

Figure S7: e) Bright field STEM and corresponding elemental maps of Ir, Sb and Sn, and FFT image from quenched 51-ISS-Q.

OER kinetics and stability (Fig. S8) of 51-ISS-Q were comparable to 51-ISS. The emergence of a redox couple at 0.8 V (vs. RHE) during the first cycle (Fig. S5a), which shifted positively with each subsequent cycle, indicates the growth of a hydrous Ir layer. This behaviour is consistent with observations made in other studies.[7, 8] The high concentration of surface Ir nanoparticles served as active sites, in addition to high intrinsic activity of electrochemically grown hydrous Ir oxides.[9, 10]

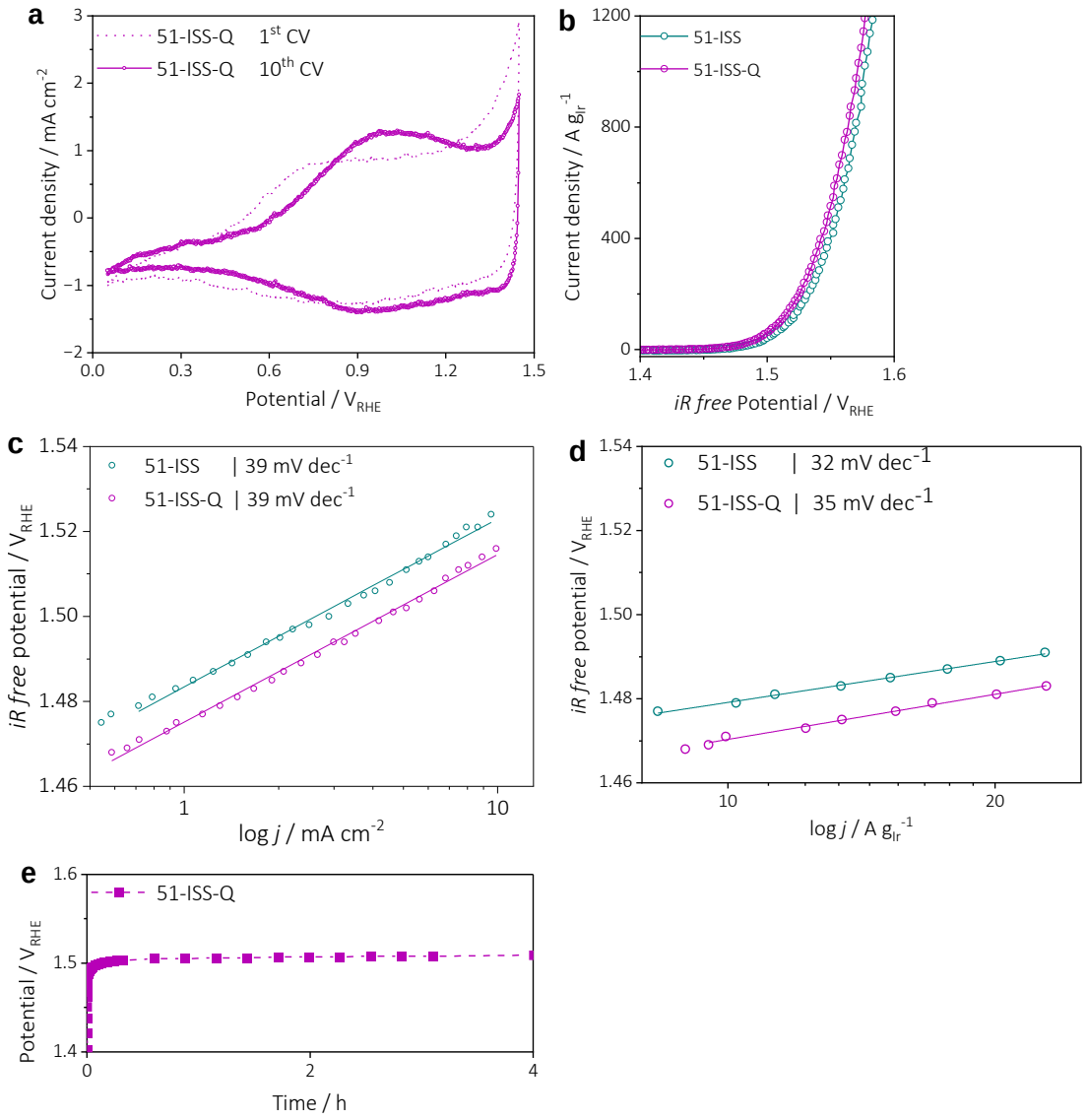

Figure S8: RDE measurements of quenched 51-ISS-Q compared with unquenched 51-ISS. a) Cyclic voltammogram b) Ir-mass specific OER activity plot. c) electrode area-normalized Tafel plot. d) mass-normalized Tafel plot. e) Chronopotentiometry at 10 mA cm^{-2} for 4 h.

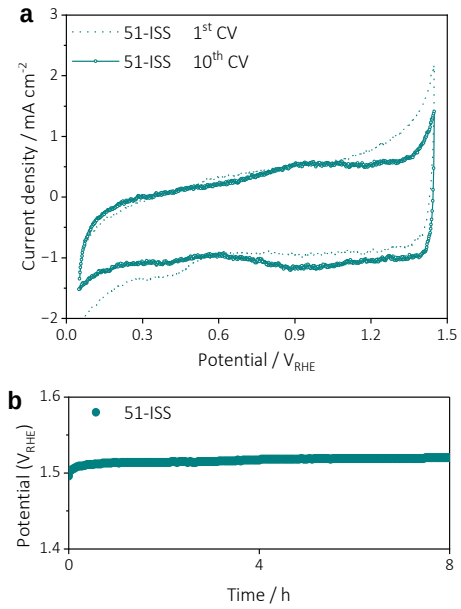

Figure S10: RDE measurements of 51-ISS. a) Cyclic voltammogram. b) Chronopotentiometry at 10 mA cm^{-2} for 8 h.

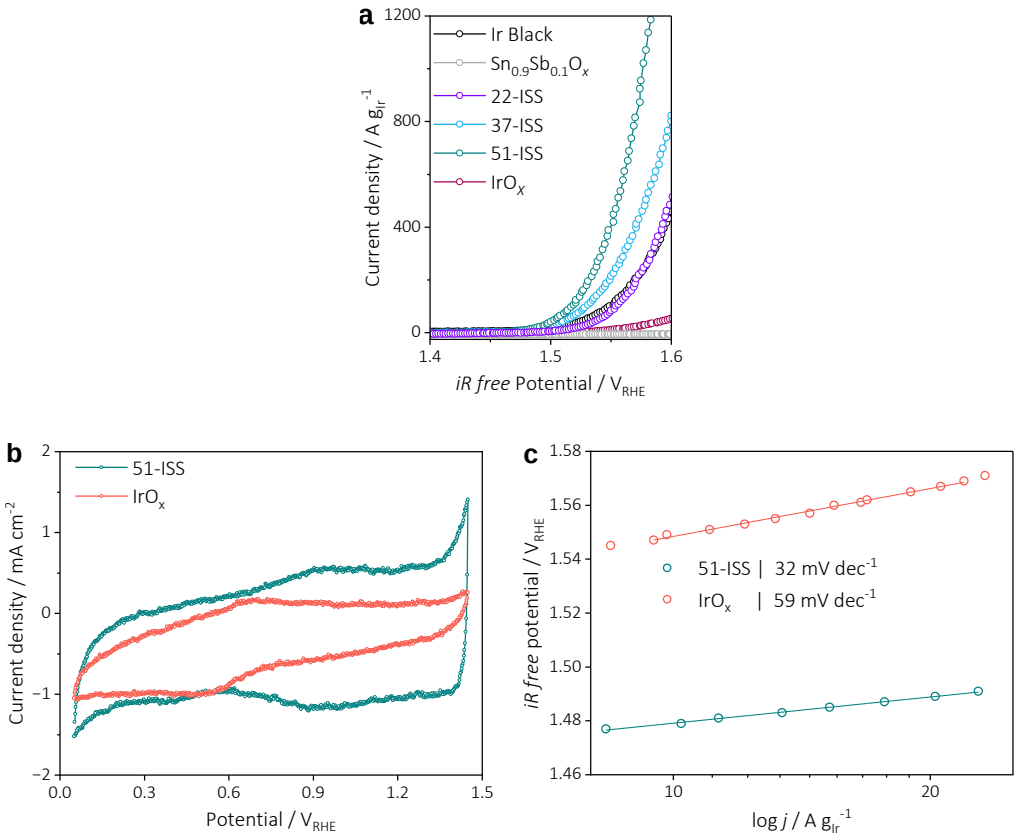

Figure S9: a) Ir-mass specific OER activity plot for FSP-made $Sn_{0.9}Sb_{0.1}O_x$ (0 wt.% Ir), 22-ISS (20 wt.% Ir), 37-ISS (35 wt.%), 51-ISS (50 wt.% Ir) and IrO_x (85 wt.% Ir) in comparison with commercial Ir black. b) Cyclic voltammogram of IrO_x compared with 51-ISS. c) Ir mass-normalized Tafel plot of IrO_x compared with 51-ISS.

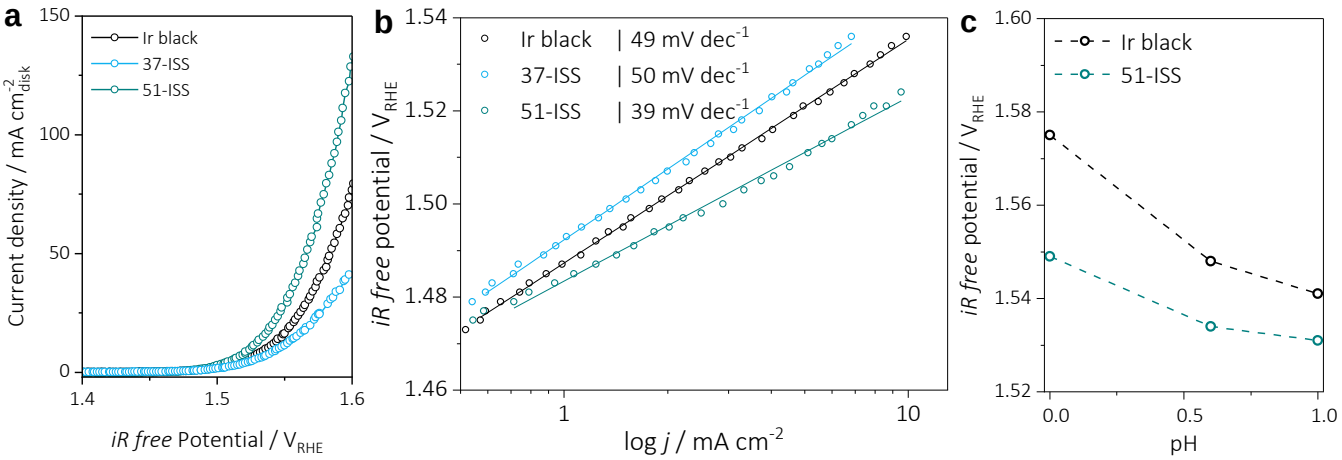

Figure S11: a) Electrode geometric area-normalized OER activity plot. b) Electrode area-normalized Tafel slope. c) pH dependence of OER potential at 50 A g^{-1} on the RHE scale in $HClO_4$ electrolytes with different pH.

TOF (in s^{-1}) can be related to the number of oxygen molecules produced per second per Ir site. For TOF calculation, the active surface redox sites were determined by integrating the anodic oxidation peak of Ir^{III} to Ir^{IV} without the capacitive current, using the following formula:[6]

$$\mathrm{TOF} = \frac{j}{\mathrm{n}\ Q_s}$$

Where j is mass activity in A g^{-1} at a particular overpotential, n is the number of electrons involved in the reaction (for example, one electron take part in the Ir^{III} to Ir^{IV} reaction), Q_s charge of the oxidation peak in A s g^{-1}, Q_{e^-} charge of an electron (1.6×10^{19}) in A s, and Ns (in g^{-1}) is the number of active surface atoms per gram of Ir loading,

$$\text{Number of active atoms } (N_s) = \frac{Q_s}{Q_{e^-}}$$

Table S2: Number of active atoms per gram, molar specific active sites, and molar specific activity

Sample	N_s / g^{-1}	Molar specific active sites / mol g^{-1}	Molar specific activity at 0.23 V and 0.33 V / A $mmol^{-1}$
Ir black	$2.22 \cdot 10^{22}$	0.037	0.24 and 26.0
37-ISS	$5.32 \cdot 10^{22}$	0.088	0.11 and 16.3
51-ISS	$7.03 \cdot 10^{22}$	0.117	0.10 and 25.3

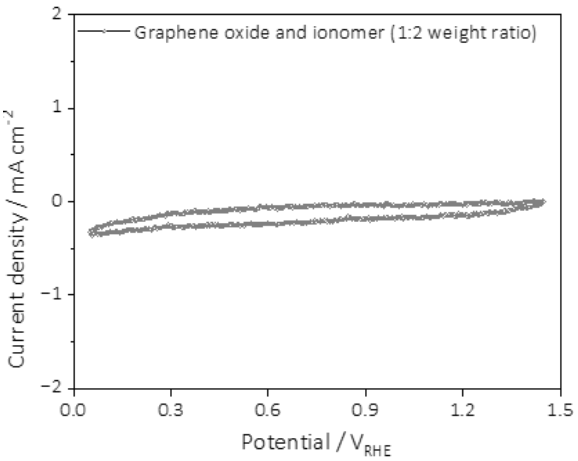

Figure S12: RDE Cyclic voltammogram measurements of Graphene oxide using the composition similar to interlayer (IL).

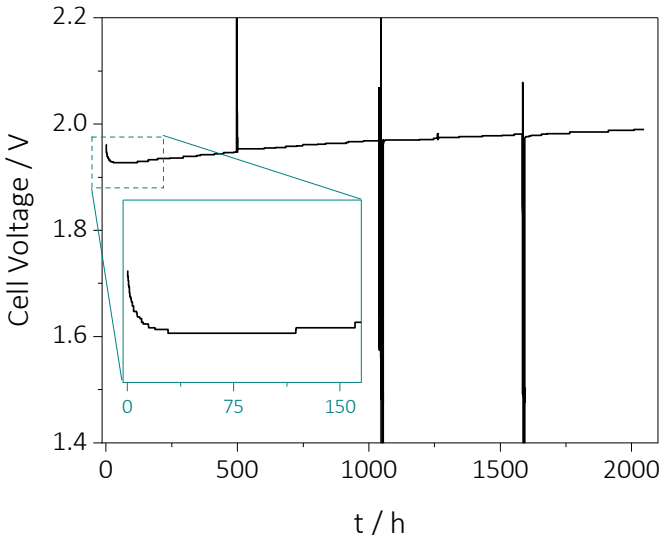

Figure S13: 2000 h durability test in the PEMWE cell. At around 500 h the cell was interrupted for test bench maintenance activity and at 1038 and 1560 h for diagnostic tests. Inset in the figure zooms in the cell voltage response during the first 165 h.

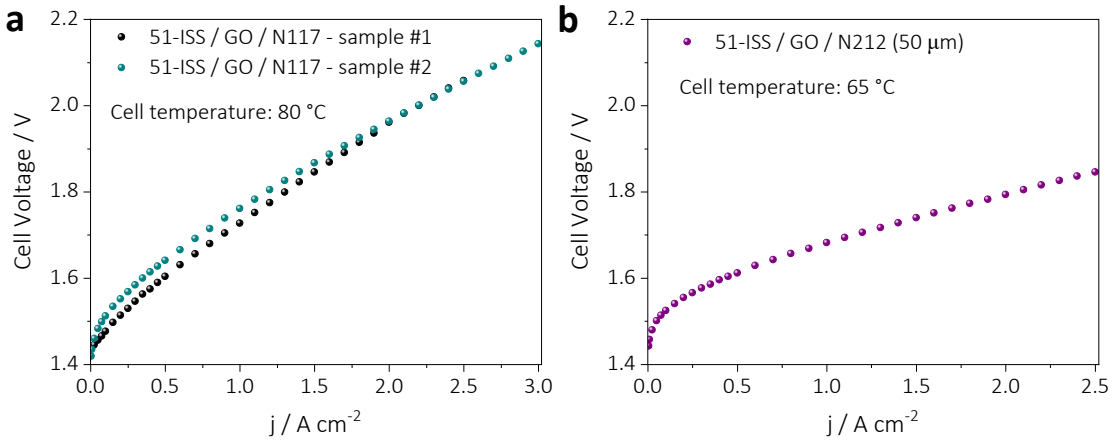

Figure S14: Polarization curves recorded for 51-ISS: a) using Nafion 117 membrane and b) Nafion 212 membrane.

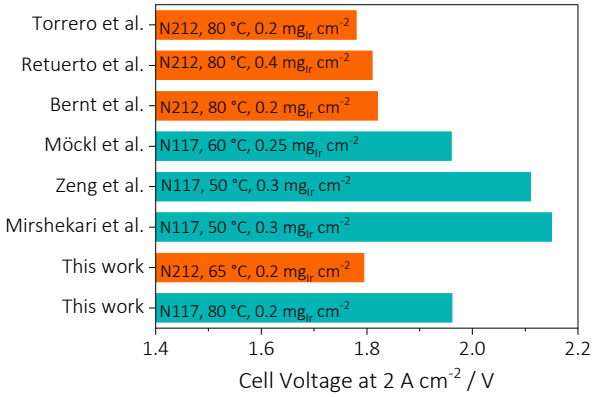

Figure S15: Comparison of performance of MEAs with 51-ISS electrocatalyst to studies by Mirshekari et al.,[11] Zeng et al.,[12] Möckl et al.,[13] Bernt et al.,[14] Retuerto et al.,[15] and Torrero et al.,[16] with with low loaded (≤ 0.3 mg cm^{-2}) PEMWE that showed durability over long term (≥ 500 h) at a nominal current density of (≥ 2 A cm^{-2}).

Table S3: 51-ISS performance comparison to studies with low-loaded (≤ 0.3 mg cm^{-2}) PEMWE that showed durability over long-term operation (≥ 500 h) at a nominal current density of ≥ 2 A cm^{-2}. Note the different membranes used in each study.

OER catalyst	Ir load / mg cm^{-2}	Membrane (thickness in µm)	T / °C	Initial cell voltage at 2 A cm^{-2} / V	Cell voltage degradation rate* / µV h^{-1}	Expected cell voltage after 10k hours** / V	Ref.	Year of publica-tion
51-ISS	0.2	N117 (183)	80	1.961	18 (1500-2000 h)	**2.14**	This work	
		N212 (50)	65	1.794		**1.97**		
IrO_2	0.2	N117	80	1.910	34 (500-1000 h)	**2.25**		
Ir black	0.2	N117	80	1.950	41 (100-500 h)	**2.36**		
TiO_2@$IrO(OH)_x$	0.2	N212 (50)	80	1.82	1 (1000-3000 h)	**1.83**	[14]	2021
	0.25	N117 (183)	60	1.96		**1.97**	[13]	2022

Sr_2CaIrO_6	0.2	N212 (50)	80	1.78	10 (0-1000 h)	**1.88**	[16]	2023
Ir/IrO_x	0.3	N117 (183)	50	2.15	37 (0-3000 h)	**2.52**	[11]	2020
		N117 (183)	50	2.11	15 (3000-5000 h)	**2.26**	[12]	2022

* cell operation hours used for estimation of degradation rate is given in brackets. ** Expected cell voltage after 10k hours in V assuming that the cell degradation remains constant = Initial cell voltage in V + (Degradation rate in V h^{-1} x 10000 in h). Note the difference in membrane used.

Table S4: 51-ISS performance comparison to studies with low-loaded (≤ 0.3 mg cm^{-2}) PEMWE that demonstrated durability for short term operation (< 500 h).

OER catalyst	Anode PGM load / mg cm^{-2}	Membrane (thickness in µm)	T /°C	Initial cell voltage at 2 A cm^{-2} / V	Cell Voltage Degradation rate* / µV h^{-1}	Expected cell voltage after 10k hours** / V	Ref.	Year of publica-tion
IrO_2 textile	0.2	N212 (50)	80	1.725	18 (at 1 A cm^{-2})	**1.91**	[17]	2023
Sputtered Ir-Ru	0.16	N212 (50)	80	1.726	37 (at 1 A cm^{-2})	**2.10**	[18]	2023
Gold&IrO_2 bilayer	0.12	N117 (183)	80	1.97	50 (at 1 A cm^{-2})	**2.47**	[19]	2024
PtIr nanoflowers	0.07	N212 (50)	80	1.77	45 (at 0.5 A cm^{-2})	**2.22**	[20]	2024
Ir@WO_xNRs-100	0.15	N115 (127)	80	1.96	50 (at 0.5 A cm^{-2})	**2.46**	[21]	2021
Ir black, gradient tapered structured anode	0.2	N115 (127)	65	1.801	140 (at 1 A cm^{-2})	**3.20**	[22]	2022
Honeycomb Ir-coated GDL	0.27	N117 (183)	80	1.842	220 (at 1.8 A cm^{-2})	**4.04**	[23]	2023
IrO_x film on Fe_2N/Ti PTL	0.04	N115 (127)	80	1.71	368 (at 2 A cm^{-2})	**5.39**	[24]	2023
Ir-$IrO_xH_ySe_z$/HCC	0.05	N212 (50)	80	1.78	540 (at 1 A cm^{-2})	**7.18**	[25]	2024
Ir/Ru/Ti electrode	0.17	N117 (183)	80	1.92	1000 (at 1.6 V)	**11.92**	[26]	2024
TaO_x/IrO_2	0.15	N115 (127)	80	1.83	- (at 1 A cm^{-2})		[27]	2023
Nanoporous Ir-Nanosheet	0.17	N117 (183)	80	1.8	-		[3]	2021
IrO_2 with modified PTL	0.04	N117 (183)	80	1.86	-		[28]	2021
Hybrid anode IrO_2/Ir/PTL	0.09	N212 (50)	80	1.73	-		[29]	2023
TiO_2@IrO_x	0.23	N212 (50)	80	1.78	-		[30]	2024
Ir black, modified PTL	0.2	N115 (127)	80	1.93	-		[31]	2023

*Durability test condition (current or potential hold) is given in brackets. ** Expected cell voltage after 10k hours in V assuming that the cell degradation remains constant = Initial cell voltage in V + (Degradation rate in V h^{-1} x 10000 in h). Note the difference in membrane used.

Considering the differences in Ir mass loading, membrane thicknesses, cell temperatures, cell compression, pre-conditioning time, nominal current densities used for durability tests, and the length of durability tests in the literature, a direct comparison of performance and stability is challenging. Even setting these differences aside, comparing initial performance alone can be misleading due to variations in pre-condition protocols. For instance, Ir black shows impressive

initial performance during the initial hours of operation but fails to maintain steady operation long-term (Fig. S16), while, the Ir oxides-based cells required a stabilization time of up to 1000 h.[13]

Figure S16 shows that although the initial performance of commercial IrO_2 outperforms 51-ISS, this trend reverses within 24 h of operation, raising questions about the utility of comparing initial performance in PEMWE, which demands tens of thousands of hours of stable performance. Conversely, a strong linear correlation between cell voltage and logarithm of time, as demonstrated in this study (Fig. 5e), is rarely projected in the literature for PEMWE performance over 10,000 h. Therefore, in Table S3, the cell voltage after 10,000 h of operation was estimated using both initial performance and degradation rates assuming that the degradation rates remain constant over time: Initial cell voltage (V) + (Degradation rate (V h^{-1}) x 10000 h). This long-term projection offers a more reliable assessment of potential of a newly developed catalyst. It is apparent that even after 10,000 h, the FSP-made 51-ISS could perform relatively higher or equal compared to recent literature with different anode components, except for TiO_2@$IrO(OH)_x$. The literature was classified into two tables: Table S3 includes low loaded (≤ 0.3 mg cm^{-2}) PEMWE that showed durability over long term (≥ 500 h) at a nominal current density of (≥ 2 A cm-2), and Table S4 includes low loaded (≤ 0.3 mg cm^{-2}) PEMWE that demonstrated durability for short term (< 500 h).

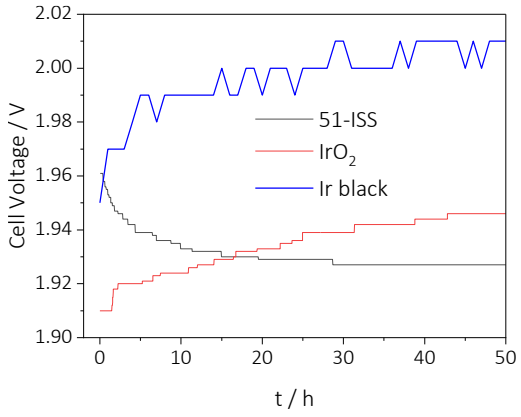

Figure S16: Comparison of short-term performance stability for 51-ISS, IrO_2, and Ir black in the PEMWE cell setup with a controlled Ir loading of 0.2 mg cm^{-2} operated at a nominal current density of 2 A cm^{-2}.

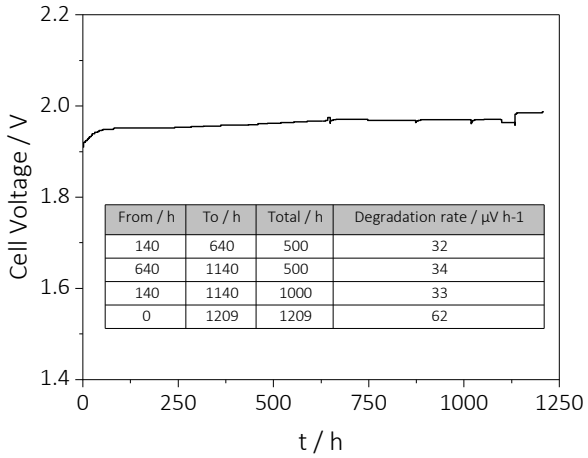

Figure S17: Durability test for commercial IrO_2 in the PEMWE cell setup with a controlled Ir loading of 0.2 mg cm^{-2} for 1209 h at 2 A cm^{-2}. The same setup as shown in the inset of Fig. 6a was used. Inset: Degradation rates at different intervals (140 to 640 h, 640 to 1140 h, and 140 to 1140 h) and for the whole duration of 1209 h.

Table S5: Performance and degradation comparison at 2 A cm^{-2} for commercial IrO_2 and Ir black and the FSP-made 51-ISS in the PEMWE cell setup with a controlled Ir loading of 0.2 mg cm^{-2} . Note that the cell voltage values at specific intervals were taken from durability tests (Fig. 5a and Fig. S18).

Cell running time / h	**Cell Voltage at 2 A cm^{-2} / V**		
	Commercial IrO_2	51-ISS	Ir black
0	1.910	1.961	1.950
140	1.952	1.930	1.99
500	1.962	1.947	2.01 (EOT)
640	1.968	1.955	
1140	1.985	1.970	
1209	1.987 (EOT)	1.971	
2000		1.989 (EOT)	

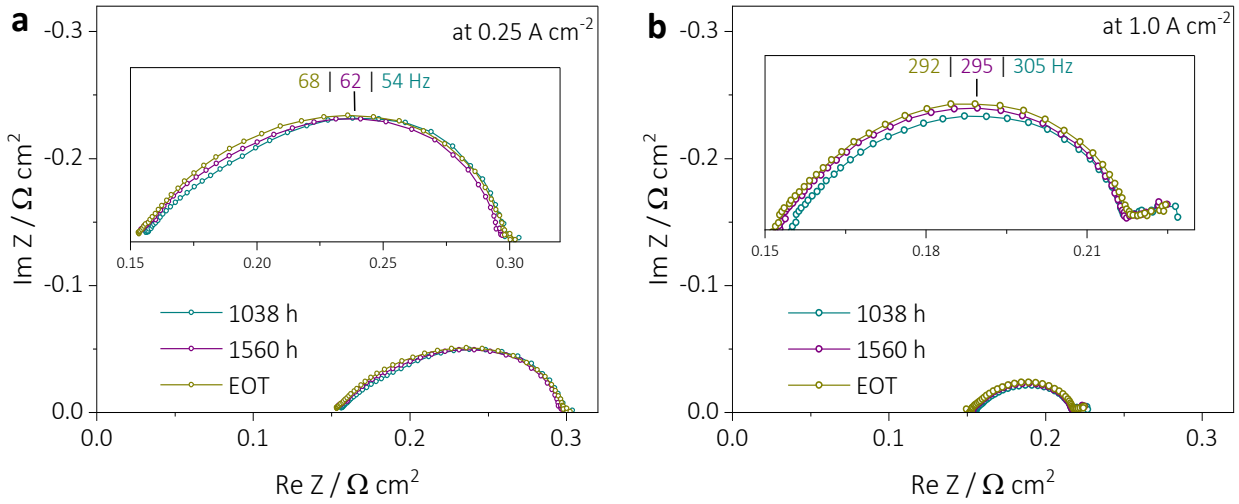

Figure S19: PEMWE cell measurements: EIS Nyquist plot of the cell resistance at a) 0.25 A cm^{-2} and b) 1 A cm^{-2}.

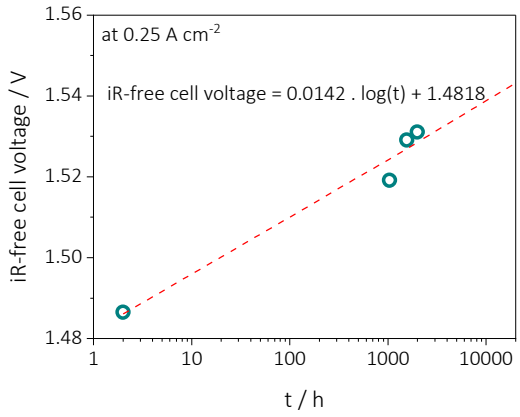

Figure S18: iR-free cell voltage at 0.25 A cm^{-2} versus the logarithmic of time plot. The dashed red lines are linear regression fits for the respective plots.

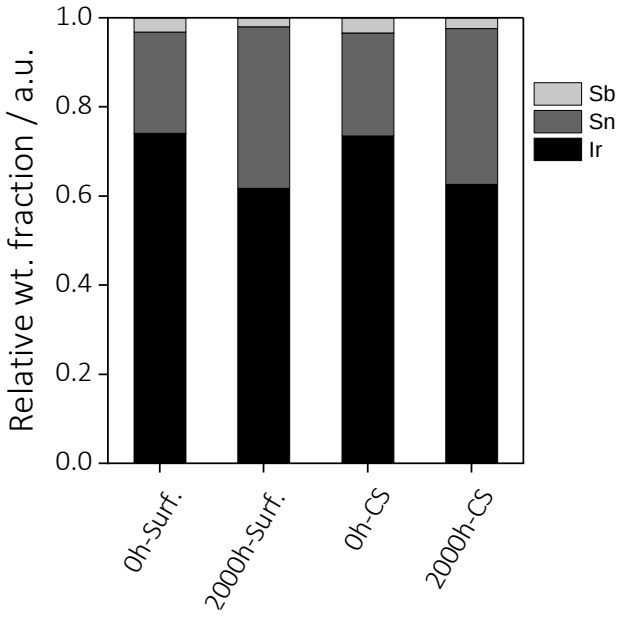

Figure S20: Relative weight fraction of Ir, Sn and Sb, on CL surface (surf.) and cross section (CS) of a pristine and the 2000 h operated CCMs, derived from energy dispersive x-ray analysis.

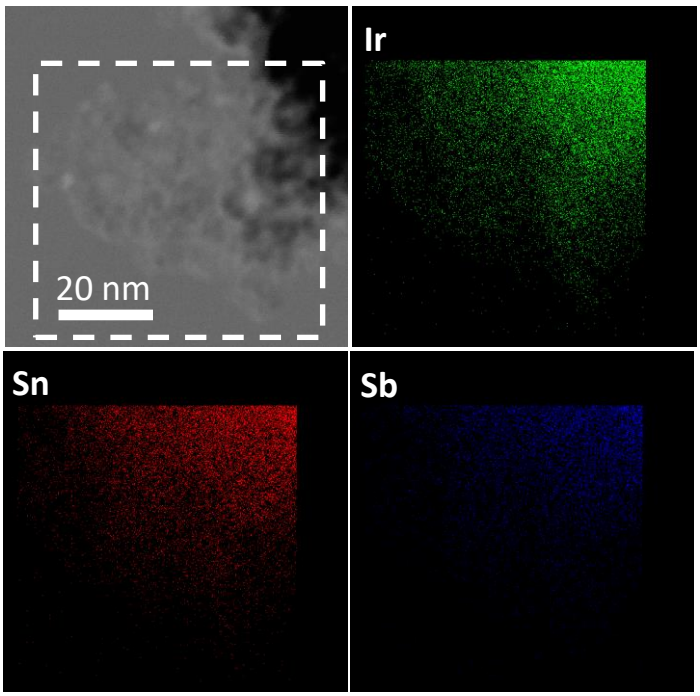

Figure S21: TEM post-test analysis for the catalyst sample collected from the 2000 h tested anode CCM. TEM image and corresponding EDX mapping of Ir, Sn and Sb.

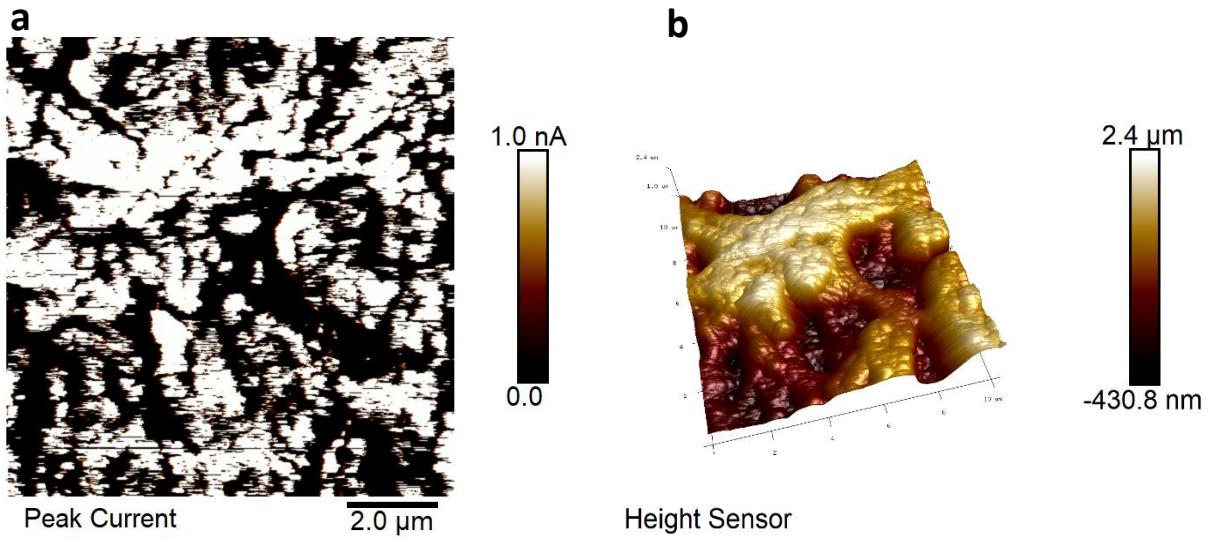

Figure S22: a) AFM electronic conductivity measurement on the pristine anode CL with 51-ISS. b) the corresponding height measurement.

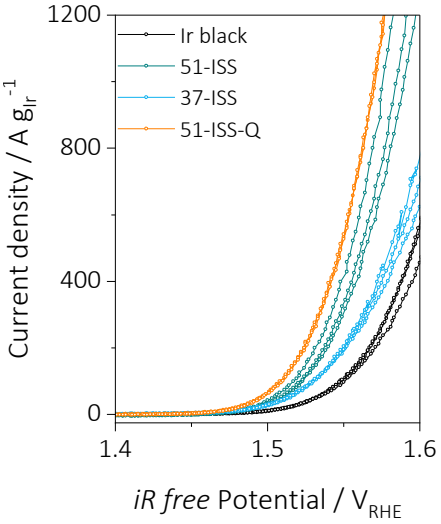

Figure S23: Three representative RDE measurements were shown for 51-ISS, 37-ISS and 51-ISS-Q in comparison with Ir black.

References

[1] Sahm, T.; Mädler, L.; Gurlo, A.; Barsan, N.; Pratsinis, S. E.; Weimar, U. Flame spray synthesis of tin dioxide nanoparticles for gas sensing. *Sensor Actuat B-Chem* **2004**, *98* (2-3), 148-153. DOI: 10.1016/j.snb.2003.10.003.
[2] Blattmann, C. O.; Güntner, A. T.; Pratsinis, S. E. In Situ Monitoring of the Deposition of Flame-Made Chemoresistive Gas-Sensing Films. *Acs Appl Mater Inter* **2017**, *9* (28), 23926-23933. DOI: 10.1021/acsami.7b04530.
[3] Chatterjee, S.; Peng, X.; Intikhab, S.; Zeng, G. S.; Kariuki, N. N.; Myers, D. J.; Danilovic, N.; Snyder, J. Nanoporous Iridium Nanosheets for Polymer Electrolyte Membrane Electrolysis. *Adv Energy Mater* **2021**, *11* (34). DOI: 10.1002/aenm.202101438.
[4] Muravev, V.; Parastaev, A.; van den Bosch, Y.; Ligt, B.; Claes, N.; Bals, S.; Kosinov, N.; Hensen, E. J. M. Size of cerium dioxide support nanocrystals dictates reactivity of highly dispersed palladium catalysts. *Science* **2023**, *380* (6650), 1174-1179. DOI: 10.1126/science.adf9082.
[5] Muravev, V.; Spezzati, G.; Su, Y. Q.; Parastaev, A.; Chiang, F. K.; Longo, A.; Escudero, C.; Kosinov, N.; Hensen, E. J. M. Interface dynamics of Pd-CeO single-atom catalysts during CO oxidation. *Nat Catal* **2021**, *4* (6), 469-478. DOI: 10.1038/s41929-021-00621-1.
[6] Lettenmeier, P.; Wang, L.; Golla-Schindler, U.; Gazdzicki, P.; Cañas, N. A.; Handl, M.; Hiesgen, R.; Hosseiny, S. S.; Gago, A. S.; Friedrich, K. A. Nanosized IrOx-Ir Catalyst with Relevant Activity for Anodes of Proton Exchange Membrane Electrolysis Produced by a Cost-Effective Procedure. *Angew Chem Int Edit* **2016**, *55* (2), 742-746. DOI: 10.1002/anie.201507626.
[7] Wang, L.; Lettenmeier, P.; Golla-Schindler, U.; Gazdzicki, P.; Canas, N. A.; Morawietz, T.; Hiesgen, R.; Hosseiny, S. S.; Gago, A. S.; Friedrich, K. A. Nanostructured Ir-supported on Ti4O7 as a cost-effective anode for proton exchange membrane (PEM) electrolyzers. *Physical Chemistry Chemical Physics* **2016**, *18* (6), 4487-4495. DOI: 10.1039/c5cp05296c.
[8] Reier, T.; Oezaslan, M.; Strasser, P. Electrocatalytic Oxygen Evolution Reaction (OER) on Ru, Ir, and Pt Catalysts: A Comparative Study of Nanoparticles and Bulk Materials. *Acs Catal* **2012**, *2* (8), 1765-1772. DOI: 10.1021/cs3003098.
[9] Hartig-Weiss, A.; Miller, M.; Beyer, H.; Schmitt, A.; Siebel, A.; Freiberg, A. T. S.; Gasteiger, H. A.; El-Sayed, H. A. Iridium Oxide Catalyst Supported on Antimony-Doped Tin Oxide for High Oxygen Evolution Reaction Activity in Acidic Media. *Acs Appl Nano Mater* **2020**, *3* (3), 2185-2196. DOI: 10.1021/acsanm.9b02230.
[10] Oh, H. S.; Nong, H. N.; Reier, T.; Bergmann, A.; Gliech, M.; de Araujo, J. F.; Willinger, E.; Schlogl, R.; Teschner, D.; Strasser, P. Electrochemical Catalyst-Support Effects and Their Stabilizing Role for IrOx Nanoparticle Catalysts during the Oxygen Evolution Reaction. *Journal of the American Chemical Society* **2016**, *138* (38), 12552-12563. DOI: 10.1021/jacs.6b07199.
[11] Mirshekari, G.; Ouimet, R.; Zeng, Z. Q.; Yu, H. R.; Bliznakov, S.; Bonville, L.; Niedzwiecki, A.; Capuano, C.; Ayers, K.; Maric, R. High-performance and cost-effective membrane electrode assemblies for advanced proton exchange membrane water electrolyzers: Long-term durability assessment. *International Journal of Hydrogen Energy* **2021**, *46* (2), 1526-1539. DOI: 10.1016/j.ijhydene.2020.10.112.
[12] Zeng, Z. Q.; Ouimet, R.; Bonville, L.; Niedzwiecki, A.; Capuano, C.; Ayers, K.; Soleymani, A. P.; Jankovic, J.; Yu, H. R.; Maric, R.; et al. Degradation Mechanisms in Advanced MEAs for

PEM Water Electrolyzers Fabricated by Reactive Spray Deposition Technology. *Journal of the Electrochemical Society* **2022**, *169* (5). DOI: 10.1149/1945-7111/ac7170.
[13] Mockl, M.; Ernst, M. F.; Kornherr, M.; Allebrod, F.; Bernt, M.; Byrknes, J.; Eickes, C.; Gebauer, C.; Moskovtseva, A.; Gasteiger, H. A. Durability Testing of Low-Iridium PEM Water Electrolysis Membrane Electrode Assemblies. *Journal of the Electrochemical Society* **2022**, *169* (6). DOI: 10.1149/1945-7111/ac6d14.
[14] Bernt, M.; Schramm, C.; Schroter, J.; Gebauer, C.; Byrknes, J.; Eickes, C.; Gasteiger, H. A. Effect of the IrOx Conductivity on the Anode Electrode/Porous Transport Layer Interfacial Resistance in PEM Water Electrolyzers. *Journal of the Electrochemical Society* **2021**, *168* (8). DOI: 10.1149/1945-7111/ac1eb4.
[15] María Retuerto, L. P., Jorge Torrero, Mohamed Abdel Salam, Álvaro Tolosana-Moranchel, Diego Gianolio, Pilar Ferrer, Paula Kayser, Vincent Wilke, Svenja Stiber, Verónica Celorrio, Mohamed Mokthar, Daniel García Sanchez, Aldo Saul Gago, Kaspar Andreas Friedrich, Miguel Antonio Peña, José Antonio Alonso & Sergio Rojas. Highly active and stable OER electrocatalysts derived from Sr2MIrO6 for proton exchange membrane water electrolyzers. *Nature communication* **2022**, *13:7935*. DOI: doi.org/10.1038/s41467-022-35631-5.
[16] Torrero, J.; Morawietz, T.; Sanchez, D. G.; Galyamin, D.; Retuerto, M.; Martin-Diaconescu, V.; Rojas, S.; Alonso, J. A.; Gago, A. S.; Friedrich, K. A. High Performance and Durable Anode with 10-Fold Reduction of Iridium Loading for Proton Exchange Membrane Water Electrolysis. *Adv Energy Mater* **2023**, *13* (23). DOI: 10.1002/aenm.202204169.
[17] Higashi, S.; Beniya, A. Ultralight conductive IrO2 nanostructured textile enables highly efficient hydrogen and oxygen evolution reaction: Importance of catalyst layer sheet resistance. *Appl Catal B-Environ* **2023**, *321*. DOI: 10.1016/j.apcatb.2022.122030.
[18] Hrbek, T.; Kús, P.; Kosto, Y.; Rodríguez, M. G.; Matolínová, I. Magnetron-sputtered thin-film catalyst with low-Ir-Ru content for water electrolysis: Long-term stability and degradation analysis. *Journal of Power Sources* **2023**, *556*. DOI: 10.1016/j.jpowsour.2022.232375.
[19] Shi, Y.; Ding, C.; Lu, Z. X.; Shen, L. S.; Huang, K.; Zhao, C. L.; Tan, H. Y.; Yan, C. F. Tuning the In-Plane Electrical Conductivity and Performance of the Low Ir Anode in a Proton Exchange Membrane Water Electrolyzer. *Acs Sustain Chem Eng* **2023**, *12* (1), 423-432. DOI: 10.1021/acssuschemeng.3c06209.
[20] Qin, J. Q.; Lv, Y.; Han, G. Q.; Liu, H. Y.; Li, Y. P.; Zhang, H. Y.; Zhou, X. Y.; Xing, K. R.; Li, T. T.; Sun, C. Y.; et al. Integrated ultra-low PtIr catalyst coated membrane toward efficient proton exchange membrane water electrolyzers. *Chemical Engineering Journal* **2024**, *479*. DOI: 10.1016/j.cej.2023.147913.
[21] Jiang, G.; Yu, H. M.; Li, Y. H.; Yao, D. W.; Chi, J.; Sun, S. C.; Shao, Z. G. Low-Loading and Highly Stable Membrane Electrode Based on an Ir@WO NR Ordered Array for PEM Water Electrolysis. *Acs Appl Mater Inter* **2021**, *13* (13), 15073-15082. DOI: 10.1021/acsami.0c20791.
[22] Dong, S.; Zhang, C. Y.; Yue, Z. Y.; Zhang, F. R.; Zhao, H.; Cheng, Q. Q.; Wang, G. L.; Xu, J. F.; Chen, C.; Zou, Z. Q.; et al. Overall Design of Anode with Gradient Ordered Structure with Low Iridium Loading for Proton Exchange Membrane Water Electrolysis. *Nano Letters* **2022**, *22* (23), 9434-9440. DOI: 10.1021/acs.nanolett.2c03461.
[23] Ding, L.; Wang, W. T.; Xie, Z. Q.; Li, K.; Yu, S. L.; Capuano, C. B.; Keane, A.; Ayers, K.; Zhang, F. Y. Highly Porous Iridium Thin Electrodes with Low Loading and Improved Reaction Kinetics for Hydrogen Generation in PEM Electrolyzer Cells. *Acs Appl Mater Inter* **2023**, *15* (20), 24284-24295. DOI: 10.1021/acsami.2c23304.

[24] Jeong, H. Y.; Oh, J.; Yi, G. S.; Park, H. Y.; Cho, S. K.; Jang, J. H.; Yoo, S. J.; Park, H. S. High-performance water electrolyzer with minimum platinum group metal usage: Iron nitride-iridium oxide core-shell nanostructures for stable and efficient oxygen evolution reaction. *Appl Catal B-Environ* **2023**, *330*. DOI: 10.1016/j.apcatb.2023.122596.
[25] Kim, M. G.; Lee, H. J.; Lee, T. K.; Lee, E. J.; Jin, H. E.; Park, J. H.; Cho, S. Y.; Lee, S. H.; Ham, H. C.; Yoo, S. J. Iridium Selenium Oxyhydroxide Shell for Polymer Electrolyte Membrane Water Electrolyzer with Low Ir Loading. *Acs Energy Letters* **2024**, *9* (6), 2876-2884. DOI: 10.1021/acsenergylett.4c00884.
[26] Yasutake, M.; Noda, Z.; Matsuda, J.; Lyth, S. M.; Nishihara, M.; Ito, K.; Hayashi, A.; Sasaki, K. Ru-core Ir-shell electrocatalysts deposited on a surface-modified Ti-based porous transport layer for polymer electrolyte membrane water electrolysis. *International Journal of Hydrogen Energy* **2024**, *49*, 169-183. DOI: 10.1016/j.ijhydene.2023.07.048.
[27] Wang, Y. N.; Zhang, M. C.; Kang, Z. Y.; Shi, L.; Shen, Y. C.; Tian, B. Y.; Zou, Y. C.; Chen, H.; Zou, X. X. Nano-metal diborides-supported anode catalyst with strongly coupled TaO_x/IrO_2 catalytic layer for low-iridium-loading proton exchange membrane electrolyzer. *Nat Commun* **2023**, *14* (1). DOI: 10.1038/s41467-023-40912-8.
[28] Peng, X.; Satjaritanun, P.; Taie, Z.; Wiles, L.; Keane, A.; Capuano, C.; Zenyuk, I. V.; Danilovic, N. Insights into Interfacial and Bulk Transport Phenomena Affecting Proton Exchange Membrane Water Electrolyzer Performance at Ultra-Low Iridium Loadings. *Adv Sci* **2021**, *8* (21). DOI: 10.1002/advs.202102950.
[29] Yasutake, M.; Noda, Z.; Matsuda, J.; Lyth, S. M.; Nishihara, M.; Ito, K.; Hayashi, A.; Sasaki, K. Hybrid Anode Design of Polymer Electrolyte Membrane Water Electrolysis Cells for Ultra-High Current Density Operation with Low Platinum Group Metal Loading. *Journal of the Electrochemical Society* **2023**, *170* (12). DOI: 10.1149/1945-7111/ad1165.
[30] Hoffmeister, D.; Finger, S.; Fiedler, L.; Ma, T. C.; Körner, A.; Zlatar, M.; Fritsch, B.; Bodnar, K. W.; Carl, S.; Götz, A.; et al. Photodeposition-Based Synthesis of TiO@IrO Core-Shell Catalyst for Proton Exchange Membrane Water Electrolysis with Low Iridium Loading. *Adv Sci* **2024**. DOI: 10.1002/advs.202402991.
[31] Rogler, M.; Suermann, M.; Wagner, R.; Thiele, S.; Straub, J. Advanced Method for Voltage Breakdown Analysis of PEM Water Electrolysis Cells with Low Iridium Loadings. *Journal of the Electrochemical Society* **2023**, *170* (11). DOI: 10.1149/1945-7111/ad0b74.